

## applied optics

# Fabrication of microgrooves in PMN-PT using femtosecond laser irradiation and acid etching

TIANLUN SHEN,1 JINHAI SI,1,\* TAO CHEN,1 YONGYONG ZHUANG,2 AND XUN HOU1

<sup>1</sup>Key Laboratory for Physical Electronics and Devices of the Ministry of Education & Shaanxi Key Lab of Information Photonic Technique, School of Electronic Science and Engineering, Xi'an Jiaotong University, No. 28, Xianning West Road, Xi'an, 710049, China <sup>2</sup>Electronic Materials Research Laboratory, Key Laboratory of the Ministry of Education and International Center for Dielectric Research, School of Electronic Science and Engineering, Xi'an Jiaotong University, No. 28, Xianning West Road, Xi'an, 710049, China \*Corresponding author: jinhaisi@mail.xjtu.edu.cn

Received 30 March 2022; revised 18 June 2022; accepted 21 June 2022; posted 22 June 2022; published 15 July 2022

A simple method of fabricating Pb(Mg<sub>1/3</sub>Nb<sub>2/3</sub>)O<sub>3</sub>-PbTiO<sub>3</sub> (PMN-PT) deep grooves with high aspect ratios using an 800-nm femtosecond laser with chemical-selective etching is demonstrated. The 567-µm-deep grooves with aspect ratios of approximately 35 were obtained with no cracks or thermal affected zone. The morphologies and chemical compositions of grooves were analyzed by a scanning electron microscope with an energy dispersive x-ray spectrometer. The formation mechanism of PMN-PT grooves is attributed to the chemical reactions of hydrochloric acid (HCl) and laser-induced structural changes (LISCs). PMN-PT in LISC became amorphous or mixtures of metal oxide from crystal and all the compounds could react with concentrated HCl and form soluble matter, leaving no precipitation. Furthermore, influences of laser irradiation parameters on depths and aspect ratios of grooves are studied. © 2022 Optica Publishing Group

https://doi.org/10.1364/AO.459556

#### 1. INTRODUCTION

As a novel relaxor ferroelectric single crystal, to the best of our knowledge, Pb(Mg<sub>1/3</sub>Nb<sub>2/3)</sub>O<sub>3</sub>-PbTiO<sub>3</sub> (PMN-PT) has considerable advantages such as ultrahigh electromechanical coupling factors, piezoelectric coefficients, and so on, making it an excellent candidate in the applications of microelectron mechanical systems (MEMS) including a variety of sensing and actuating devices [1-5]. Microstructure micromachine techniques play an important role in PMN-PT applications, e.g., piezoelectric actuators require cutting PMN-PT with sharp edges and low roughness; ultrasound transducers need to manufacture microgroove arrays with small gaps and high depths [6-9]. Common methods of fabricating PMN-PT high-aspect-ratio (AR) deep grooves include wet etching [10] and dry etching [11]. For PMN-PT, the wet-etching process in particular limits the groove steepness and has no ability to fabricate devices with high ARs and small gaps. Dry etching can realize structures with high accuracy, but is limited by the drawbacks of time consumption, expensive equipment, and necessity for etching masks. Compared to the above common methods, laser micromachining has significant advantages of noncontact processing, fast removal rates, and being mask free. Nevertheless, the fabrication resolution of laser machining microstructures is relatively low [12].

In contrast to traditional laser processing techniques, e.g., long pulse lasers (>10 ps) or continuous lasers, the pulse

width of femtosecond lasers is shorter than the thermal relaxation time (e.g., metal ~10 ps) [13]. Therefore, there is no thermal effect in the deposition time range of femtosecond single pulse lasers, and the generation and diffusion of thermal effects are limited [14,15]. However, during the deposition time range of a traditional single pulse laser, photon energy is continuously absorbed, and deposited energy is transformed into heat energy in the form of phonons to realize thermal effects such as material melting and vaporization. Due to the influence of thermal effects, heat energy diffuses from the laser focusing region to the surroundings, causing serious thermal damage to the edge. Therefore, compared with traditional lasers, femtosecond laser processing can achieve sub-wavelength machining accuracies owing to its minimum heat-affected zone [16]. Piredda et al. [17] cut 200-µm-thick PMN-PT with sharp and well-defined edges using a femtosecond laser. The width of the gap decreased from top to bottom, and the minimum gap was 15 µm. However, this method has drawbacks of relatively low AR, V-shaped cut walls, repeated scanning, and low microstructure definition. Furthermore, a high laser fluence is needed in cutting thick PMN-PT or fabricating deep grooves, which results easily in defects such as cracks. By using chemical etching assisted femtosecond laser irradiation, Chen et al. realized well-defined deep grooves with high ARs in silicon and silicon carbide [18-22]. This method can be applied for high-AR and deep groove fabrication under low laser power, which can avoid cracks caused by high laser power and improve

microstructure quality. However, PMN-PT has more complex element contents and is more brittle than silicon and silicon carbide, so it is unknown whether the method of chemical etching assisted femtosecond laser irradiation is applicable.

In this study, we demonstrate a simple method of fabricating high-AR microgrooves in PMN-PT using chemical-selective etching assisted femtosecond laser irradiation. In this method, a high-AR structural change was first induced in PMN-PT by 800-nm femtosecond laser irradiation, and subsequently removed by concentrated hydrochloric acid (HCl); 567- $\mu$ m-deep grooves having ARs of 35 were fabricated with a laser power of 80 mW and scanning velocity of 0.5  $\mu$ m · s $^{-1}$ . A scanning electron microscope (SEM) equipped with an energy dispersive x-ray spectrometer (EDS) was used to analyze morphologies as well as chemical compositions of laser-induced structural change (LISC) zones and PMN-PT grooves. Furthermore, we systematically investigate the dependencies of the groove ARs on the numerical aperture (NA) of the microscope objective lens, laser average powers, and laser scanning velocity.

#### 2. EXPERIMENTAL SETUP

The schematic diagram of the fabrication procedure of PMN-PT groove structures using the chemical-selective etching assisted femtosecond laser irradiation method is shown in Fig. 1. The light source was an amplified Ti:sapphire femtosecond laser system (Libra–USP–HE, Coherent Inc., USA) with a pulse duration of 50 fs, central wavelength of 800 nm, and repetition rate of 1 kHz. A variable attenuator and mechanical shutter were used to adjust the laser power and control laser access, respectively.

0.7PMN-0.3PT single crystals provided by Xi'an Jiaotong university fabricated by the Bridgman method were used as samples in our experiments. The crystals were cut and polished into wafers with the size of  $10 \text{ mm} \times 2 \text{ mm} \times 0.7 \text{ mm}$  and orientations were along [001]. First, the sample was ultrasonically cleaned in alcohol and deionized water for 10 min each, and then placed on a computer-controlled three-dimensional (3D) XYZ movable stage (ProScanIITM, Prior Scientific Inc., UK). The laser was kept focused on the surface of the sample by a 10× microscope objective lens (NA of 0.3, Nikon). The full-width-half-maximum (FWHM) diameter of the focal spot was approximately 3.2 µm. The fabrication process was monitored via a computer screen connected to a charge-coupled device (CCD) camera. As shown in Fig. 1, the laser writing direction is along the x direction, and the polarization is linear and perpendicular to the writing direction in all experiments, unless explicitly stated otherwise. After laser irradiation, the side surface of the sample was polished to any position with abrasive paper along the LISC to observe it from the side. The polished

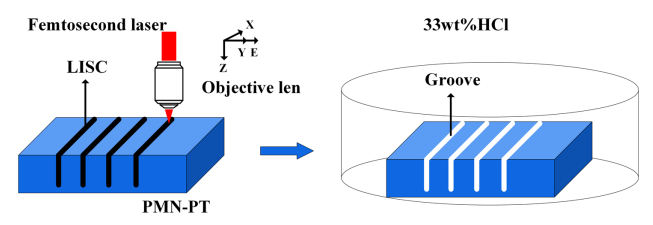


**Fig. 1.** Schematic diagram of fabricating micro-grooves in PMN-PT.

sample was ultrasonically cleaned with alcohol and deionized water for 15 min. Subsequently, the sample was etched by 33 wt. % HCl solution at room temperature for 1 h. Finally, the sample was again ultrasonically cleaned with alcohol and deionized water for 15 min each. The morphology and chemical compositions of the LISC zones and the formed grooves were characterized by a scanning electronic microscope (FEI Quanta 250 FEG Serials) equipped with an energy dispersive x-ray spectroscope (TEAMTM Serials), respectively. The crystal structures changes between LISC zones and formed grooves were characterized using a Raman system with a 50× objective lens and a 532-nm wavelength laser (Thermo Fisher Scientific).

#### 3. RESULTS AND DISCUSSION

UV-vis absorption spectra of the PMN-PT were obtained from a spectrophotometer (SHIMADZU UV-2600). As shown in Fig. 2, it is clearly seen that PMN-PT has absorption in both UV and visible light regions, and the absorption edge of PMN-PT is around 420 nm. The bandgap of PMN-PT is calculated as approximately 2.8 eV using the Tauc equation [23] and given as in inset. The results of PMN-PT UV-vis absorption spectra and calculated bandgap are similar to those in the literature [24,25].

In this work, the average power and pulse duration are measured before the focusing device. The femtosecond laser pulse duration before the focusing device measured by a commercial autocorrelator (APE, Pulsecheck) is approximately 100 fs. Figure 3 shows the morphologies and chemical compositions of the LISC region and the formed PMN-PT grooves after chemical-selective etching. The average laser power was set at 80 mW, and the scanning velocity was set at 1  $\mu$ m · s<sup>-1</sup>. As shown in Fig. 3(a), LISC zones with depths of 532 µm were formed along the transmission direction of the femtosecond laser. The LISC zone depth of 532 µm was much larger than the Rayleigh length (10 µm) of the focused femtosecond laser. This may be due to the occurrence of self-focusing by the femtosecond laser, inducing long-lasting filaments and forming such a long LISC in PMN-PT [26]. The phenomenon of an 800-nm femtosecond LISC with high depth and narrow width was similar to that in silicon and silicon carbide [18-22], but LISC depth

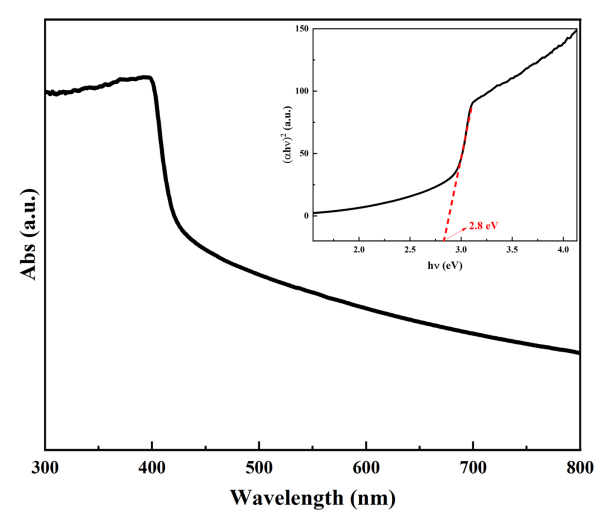


**Fig. 2.** UV-vis absorption spectra of PMN-PT; inset: calculation diagram of PMN-PT band gap.

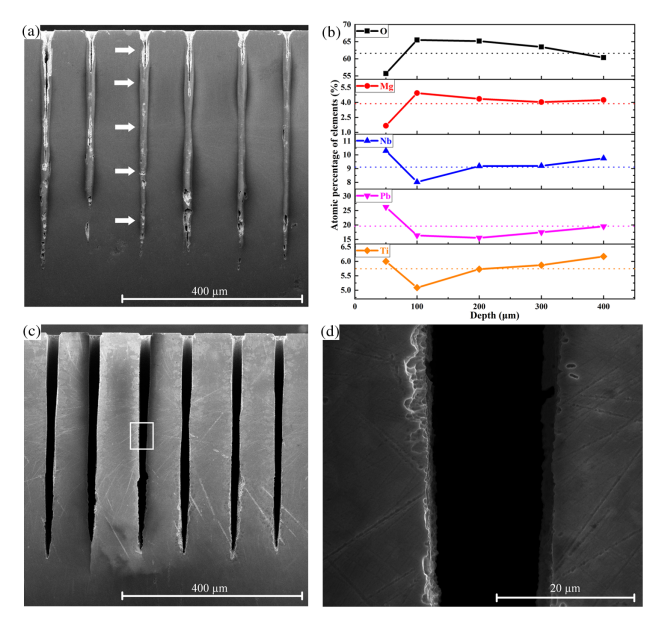


**Fig. 3.** SEM images of morphology of LISC and grooves in PMN-PT. (a) LISC. (b) Atomic percentage of elements at different depths of LISC as marked with white arrows in (a); dotted line shows the atomic percentage of elements in PMN-PT. (c) After etching with HCl. (d) Enlarged image of (c).

was much larger in PMN-PT. Because 800-nm photons cannot meet the PMN-PT bandgap energy requirements of approximately 2.8 eV, femtosecond laser-induced bond-breaking could be attributed to multiphoton absorptions. Large number of free electrons are generated at the laser focusing position due to multiphoton absorption. After a large amount of energy is absorbed by the free electrons, extremely high-temperature and highpressure plasma will form in the laser focusing region. These plasmas immediately carry out a series of complex processes, e.g., electron-phonon relaxation process, thermal diffusion process, or structural modification [27]. The LISC zone width of approximately 18 µm was larger than the FWHM diameter of the focal spot (3.2  $\mu$ m). Under the process of a 10 $\times$  objective lens (NA 0.3) and laser power of 80 mW, the effective ablation area of PMN-PT is larger than the FWHM diameter of the focal spot. In addition, the thermal accumulation effect also increases the size of LISC zones. Because of the ultra-short pulse width of a femtosecond laser, the optical deposition is a process without a thermal effect, but the thermal effect still exists in the subsequent plasma deposition process. For high-repetition-rate lasers, when the next pulse arrives at the sample, the thermal field caused by the plasma produced by the previous pulse has not been completely dissipated, resulting in thermal accumulation [28]. However, the laser repetition rate we used was 1 kHz, and the thermal accumulation effect was relatively small.

We characterized the element changes of the LISC region using an EDS spot scan. Because the groove structure is basically formed at a depth of 50  $\mu m$  in LISC zones, the EDS spot scan position at a depth of 50  $\mu m$  is selected at the edge of LISC zones to reduce the impact on EDS spot scan results of the groove morphology, e.g., test depth difference, side wall reflections, etc. The test depth of the EDS spot scan is approximately 1  $\mu m$ . The raw materials of PMN-PT are synthesized from PbO, MgO,

Nb<sub>2</sub>O<sub>5</sub>, and TiO<sub>2</sub> [29], and consisted of an oxygen element and metal elements plumbum (Pb), magnesium (Mg), niobium (Nb), and titanium (Ti). The element contents of PMN-PT are more complex than silicon and silicon carbide. Figure 3(b) shows elements at different depths of LISC after femtosecond laser irradiation, and dotted lines show the atomic percentage of elements in pristine PMN-PT. It is found that oxygen and Mg element ratios have opposite depth dependence compared to other elements. Oxygen and Mg element ratios first increased and then decreased as depth increased, whereas Ti, Nb, and Pb element ratios first decreased and then increased in LISC. At a depth of 50 µm, oxygen and Mg element ratios were lower than that in pristine PMN-PT. However, as depth increased, they became higher than that in pristine PMN-PT and reached maximum at a depth of 100 µm. However, the other metal element ratios were higher at a depth of 50 µm, but gradually became lower than that in pristine PMN-PT. Their ratios reach minimum at a depth of  $100 \mu m$ . With the increase in LISC depth, all element ratios gradually approach element ratios of the pristine PMN-PT. We can conclude that the oxygen and Mg element ratios increase but other elements decrease at a depth of 50 μm, where laser-induced grooves are formed. However, oxygen and Mg element ratios decreased, but other elements increased in the left portion of the LISC region. It may imply that oxygen and Mg elements penetrate deeper under femtosecond laser irradiation. It is known that during the interaction of a femtosecond laser and materials, extremely high-temperature and highpressure plasma will form in the laser focusing region. Oxides of Pb, Nb, and Ti at a depth of 50 µm in LISC may be evaporated and removed immediately. However, oxide of Mg may transform into high-density sintered magnesia powder because of its excellent high-temperature resistance and significantly higher melting point than oxides of Pb, Nb, and Ti [30,31]. The first decrease and then increase of magnesium and oxygen may be due to the penetration of sintered magnesium powder into the depth of LISC. In addition, the increase in the oxygen element in deeper LISC may be attributed to formation of dangling bonds induced by a femtosecond laser, which could trap foreign oxygen elements. The number of femtosecond-laser-induced dangling bonds decreased as depth increased due to the decrease in laser intensity. Hence, the oxygen concentration gradually decreased to that of PMN-PT itself.

Figure 3(c) shows sample morphologies after HCl solution etching for 1 h. The etching rate of materials in LISC zones is much higher than that in laser non-affected zones. It can be seen that the materials in LISC zones have been almost completely removed by HCl solution, while the laser non-affected zones have almost no change due to the extremely slow etching rate, and thus grooves were formed in PMN-PT. The depths and widths at the middle depth of the grooves were approximately 532 and 18 µm, respectively. The AR was calculated to approximately 28. We also conducted Raman tests on the pristine PMN-PT, LISC zones, edge part, and central part of the formed grooves. As shown in Fig. 4. Raman spectra show that the crystal structure of PMN-PT in LISC zones has been completely destroyed. However, the Raman spectra of the central and edge parts of the formed grooves are similar to the pristine PMN-PT. We believe that the material in the LISC area including heataffected zones has been basically removed by HCl solution. It

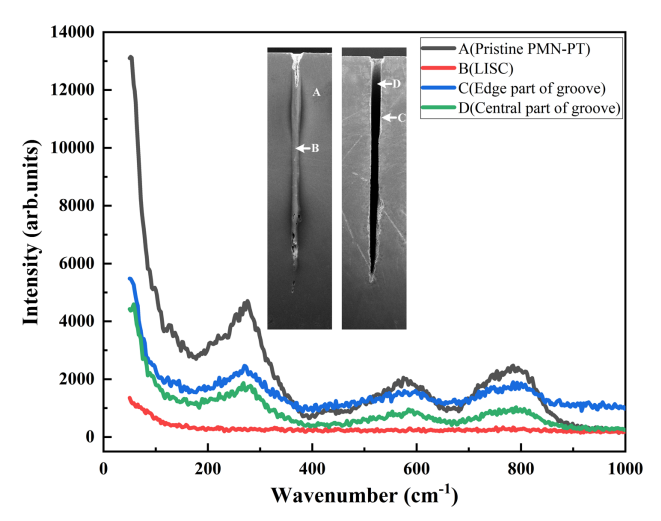


**Fig. 4.** Raman spectra of pristine PMN-PT (A), LISC zones (B), edge part (C), and central part (D) of the formed grooves. Insets shows the Raman test position.

is known that crystal PMN-PT has good chemical stability and hardly reacts with HCl solution [10]; therefore, destruction of the crystal structure made PMN-PT less stable in chemical and physical properties. PMN-PT in LISC may become amorphous or a mixture of metal oxides. The removing of LISC may be attributed to the reactions of the yield metal oxides and HCl solution. After reaction, there was no precipitation found in the reaction vessel. Even when we centrifuged the reacted HCl solution, we did not observe precipitation or nanoparticles. This implies that all the oxides reacted with HCl solution and became soluble materials. It is known that magnesium oxide and oxides of lead including PO and PO2 could react with concentrated HCl solution, while the mechanism by which oxides of niobium and titanium can be removed by HCl solution is still unclear. Hence, the related main chemical processes are accepted as follows [32,33]:

$$PbO_x + HCl(aq) \rightarrow PbCl_2(aq) + Cl_2(\uparrow) + H_2O,$$
 (1)

$$MgO + HCl(aq) \rightarrow MgCl_2(aq) + H_2O.$$
 (2)

Therefore, the materials in the LISC zone were removed, and the surrounding zones remained unchanged. HCl etching could have high selectivity for LISC and pristine PMN-PT.

Next, we studied the influence of NAs on the morphologies of the grooves. The NAs of the objective lenses were 0.15 (Nikon LU Plan Flour  $5\times$ ), 0.3 (Nikon LU Plan Flour  $10\times$ ), 0.45 (Nikon LU Plan Flour  $20\times$ ), 0.5 (Olympus LM Plan  $50\times$ ), and 0.9 (Nikon LU Plan Flour  $100\times$ ). Correspondingly, the working distances of the objective lenses were 23.5, 17.5, 4.5, 10.6, and 1 mm, respectively. The scanning velocity and laser power were set at  $1 \, \mu \text{m} \cdot \text{s}^{-1}$  and 80 mW, respectively. Figure 5 shows the dependences of depth, width, and AR on NAs. The insets show the morphologies of grooves fabricated using microscope objectives with NAs of 0.3, 0.5, and 0.9. As shown in Fig. 5(a), when NA increased from 0.15 to 0.3, groove depths increased from 493 to 522  $\mu \text{m}$  and then decreased to 60  $\mu \text{m}$  as NA increased to 0.9, while groove widths remained

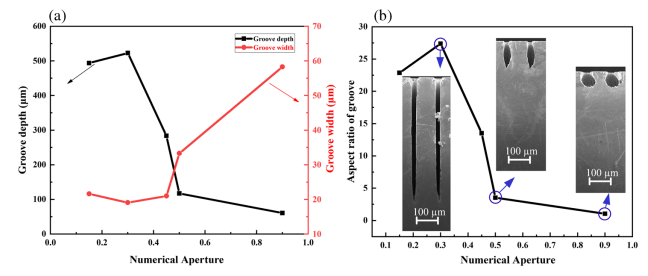


**Fig. 5.** (a) Depths, widths, and (b) aspect ratios of grooves versus NA. The grooves were fabricated by using femtosecond laser irradiation and then etched successively by 33 wt. % HCl for 1 h.

approximately 20 µm with NAs of 0.15, 0.3, and 0.45 and then increased to 58 µm as NA increased to 0.9. Figure 5(b) shows that AR has a little increase when the NA increases from 0.15 to 0.3 and then decreases as NA increases. The AR reaches a maximal value of 27 at NA of 0.3. Moreover, with the increase in NA, the cross-section shape of the groove changes from rectangular to elliptical. When the NA increases to 0.9, AR decreases to almost one. In other words, the cross sections of the grooves become almost circular. Using a larger NA objective lens, the light converges to a small spot. However, the larger the NA, the greater the energy density of the focused spot. Therefore, when using high power, a larger NA means more laser effective ablation areas will appear at the irradiated zones, which makes the groove width of the objective lens with NA of 0.9 the largest. The width of micro-grooves can decrease to the size close to the focused spot size by reducing laser power. Although the width of LISC varied with the increase in NA, the great change of AR more dominantly contributed to the depth change of LISC. It is known that both laser spot size and focus depth decrease with the increase in NA. However, femtosecond laser propagation in media also involves some nonlinear optical effects, such as self-focusing caused by the Kerr effect, self-defocusing caused by laser-induced plasma, and so on [34]. When the NA is small, the laser beam is loosely focused and femtosecond laser filamentation is more easily formed, which results in much longer depth than the laser focal depth. Since the decrease in depth is much larger than the change in width, AR of the PMN-PT grooves greatly decreases with the increase in NA. However, when NA is 0.15, the depth and AR are slightly smaller than that with NA of 0.3. This may be because the focused light intensity for NA of 0.15 is relatively weaker that for NA of 0.3, and the laser is attenuated below the damage threshold power in a shallower position. Based on the above analysis, the 10× microscope objective with NA of 0.3 was employed to fabricate high-AR grooves. In addition, laser processing is affected by spherical aberration [35]. Because the refractive index of air is different from that of PMN-PT, the laser focused by the objective lens refracts when passing through the interface between air and PMN-PT, so that the laser cannot converge at the focus, and the focus is elongated in the longitudinal direction. With the increase in processing depths in materials and NAs of objective lenses, the influence of spherical aberration on femtosecond laser processing inside materials is more serious. Since we focus the laser on the surface of PMN-PT, the spherical aberration in our experiment has little effect.

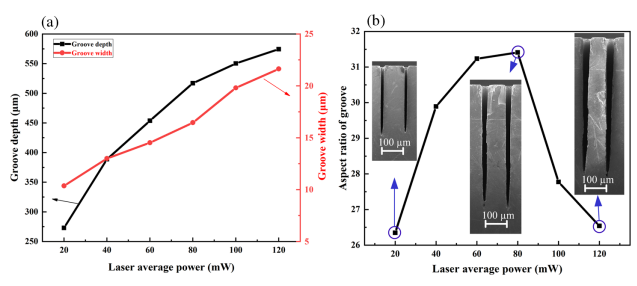


**Fig. 6.** (a) Depths, widths, and (b) aspect ratios of grooves versus laser average power. The grooves were fabricated by using femtosecond laser irradiation and then etched successively by 33 wt. % HCl for 1 h.

The influence of the laser average power on the morphologies of the grooves was also investigated. The 10× microscope objective lens with NA of 0.3 was used to focus the femtosecond laser, and the scanning velocity was set at 1  $\mu$ m · s<sup>-1</sup>. Laser average powers were varied from 20 to 120 mW with increments of 20 mW. Figure 6 shows the depths, widths, and ARs of grooves fabricated at different laser average powers, and the insets show the cross-sectional morphologies of grooves fabricated at laser average powers of 20, 80, and 120 mW. It can be seen that as the laser average power increases from 20 to 120 mW, groove depths increase from 273 to 574 µm, while groove widths increase from 10.3 to 21.6 μm. Figure 6(b) shows that AR increases when the laser power increases from 20 to 80 mW and then decreases as laser power increases. The AR reached the maximal value of 31 at a laser power of 80 mW. As mentioned above, the multiphoton absorption associated with the extreme intensity of the femtosecond pulse is responsible for the fracture of crystal bonds and subsequent formation of dangling bonds in PMN-PT. As the average power of the incident laser increases, both the laser penetrating depth and the area above damaged threshold intensity in the beam spot increase, resulting in the increase in LISC depth and width, respectively. Under the condition of low laser power, the increase rate of depth is greater than that of width with the increase in power, causing AR to increase rapidly. With a further increase in laser power, more nonlinear optical processes such as multiphoton absorption can be excited and disturb the formation of filaments in deeper regions [18]. Hence the increase rate of filament length and grooves formed by chemicalselective etching decreases, while the width still increases linearly with the increase in laser power from 20 to 120 mW. As a further consequence, the AR increases first and then decreases with the increase in laser power. Based on the above analysis, a laser power of 80 mW was employed to fabricate high-AR grooves.

Figure 7 shows the dependences of depth, width, and AR of PMN-PT grooves on laser scanning velocity. A  $10\times$  objective lens with NA 0.3 was used, and the laser average power was set to 80 mW. Scanning velocities were set to 0.5, 1, 2, 4, 6, and  $8\,\mu\text{m}\cdot\text{s}^{-1}$ . Correspondingly, the pulse densities were 2000, 1000, 500, 250, 166, and 125 pulses· $\mu\text{m}^{-1}$ . The insets show the grooves fabricated with laser scanning velocities of 0.5, 4, and  $8\,\mu\text{m}\cdot\text{s}^{-1}$  (2000, 250, and 125 pulses· $\mu\text{m}^{-1}$ , respectively). It can be seen that groove depths decreased from 567 to 370  $\mu\text{m}$  as scanning velocity increased from 0.5  $\mu\text{m}\cdot\text{s}^{-1}$  (2000 pulses· $\mu\text{m}^{-1}$ ) to  $8\,\mu\text{m}\cdot\text{s}^{-1}$  (125 pulses· $\mu\text{m}^{-1}$ ), while groove widths remained approximately 13  $\mu\text{m}$  regardless of the change in scanning velocity. The groove AR decreased from

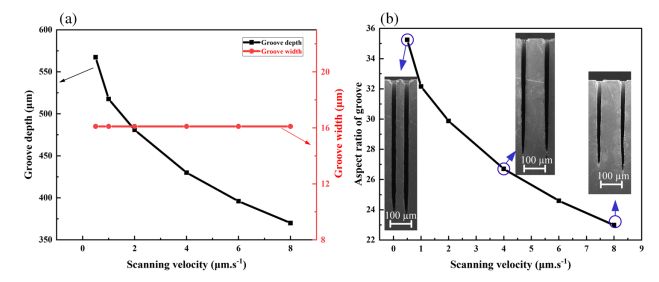


**Fig. 7.** (a) Depths, widths, and (b) aspect ratios of grooves versus scanning velocity. The grooves were fabricated by using femtosecond laser irradiation and then etched successively by 33 wt. % HCl for 1 h.

maximum 35 at  $0.5 \, \mu m \cdot s^{-1}$  (2000 pulses· $\mu m^{-1}$ ) to minimum 23 at  $8 \, \mu m \cdot s^{-1}$  (125 pulses· $\mu m^{-1}$ ). This was due to the decrease in accumulated average number of pulses in the laser irradiated area as the scanning velocity increased, which resulted in a reduction in the depth of the LISC zone. The width of the groove does not change significantly because it is determined by the laser beam size and has saturated even at the largest scanning velocity applied in our experiments.

Moreover, we studied the effect of laser polarization on the morphology and structure of formed grooves. Figure 8 shows SEM images of three different laser polarization directions in an experiment with laser power of 30 mW, scanning velocity of  $8 \, \mu \text{m} \cdot \text{s}^{-1}$ , and  $10 \times$  objective lens of 0.3 with linear polarization perpendicular (a) and parallel (b) to the writing direction; and with circular polarization (c). Under our experimental conditions, the best results are obtained in terms of depth and groove structure when perpendicular to the writing direction. Our experimental results are similar to the results of femtosecond laser processing indium phosphide crystal microgrooves in the literature [36]. The influence of laser polarization on crystal microstructure may be because the multiphoton ionization rate in the crystal is related to the relative direction between crystal orientation and laser polarization direction [37,38]. In addition, our research group has previously found that the polarization direction also has an impact on the nanoripples of the silicon carbide groove sidewall [39], but we did not find any clear nanoripples on the side wall of the formed grooves in PMN-PT, which may be caused by high laser power.

In short, we fabricated high AR microgrooves by femtosecond laser and acid etching technology. Because the final groove depends mainly on LISC, by using Bessel shaped femtosecond

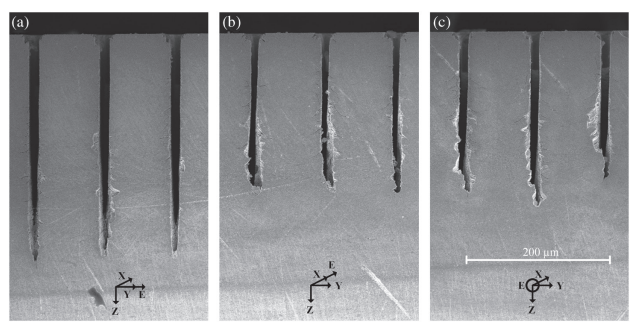


**Fig. 8.** SEM images of grooves fabricated by femtosecond laser and acid etching with three different polarization directions: (a) E perpendicular to the writing direction; (b) E parallel to the writing direction; (c) circular polarization.

laser irradiation instead of a Gaussian beam, the depth as well as AR may be further increased [40,41]. On the other hand, LISC width may be decreased to sub-micrometer by using dual-pulsed femtosecond laser Bessel beam irradiation, resulting in formation of nanogrooves after etching [42].

#### 4. CONCLUSION

In conclusion, we demonstrate a simple method to fabricate high-AR microgrooves in PMN-PT by femtosecond laser irradiation following chemical-selective etching. First, LISC zones were induced in PMN-PT, and then grooves formed after removing materials in LISC zones by HCl solution selective etching. SEM results show grooves with steep walls and no cracks or thermal affected zone. EDS results reveal that crystal PMN-PT became amorphous or a metal oxide mixture, and could react with HCl and yielded soluble substance and gas. Furthermore, the effects of NA, laser average power, and laser scanning velocity on the AR of the grooves were systematically investigated. The ARs of grooves increase first and then decrease with the increase in laser power, while ARs decrease as the scanning velocity increases. A microscope lens with a small NA should be chosen for higher-AR grooves. It is worth noting that the depths of microgrooves fabricated in SiC and Si by this method are generally less than 300 µm, and the maximum depth of PMN-PT microgrooves can reach 575 μm. Piezoelectric polymer composites with a PMN-PT microgroove array structure as the core is an important part of ultrasonic transducers. Fabrication of PMN-PT microgrooves with higher machining accuracy and higher ARs by this method is of great significance to improve the electromechanical and acoustic properties of ultrasonic sensors [9]. In addition, a PMN-PT micromechanical actuator needs to cut thick PMN-PT. Fabricating deep grooves with small gaps and steeper walls using a femtosecond laser and acid etching is also conducive to the fabrication of piezoelectric micromechanical actuators [4].

**Funding.** National Key Research and Development Program of China (2017YFB1104600); Fundamental Research Funds for the Central Universities (XJJ2016016).

**Acknowledgment.** The authors sincerely thank Ms. Dai at the International Center for Dielectric Research (ICDR) in Xi'an Jiaotong University for the support of SEM and EDS measurements and Dr. Long Hang Wang for discussion of etching PMN-PT.

**Disclosures.** The authors declare no conflicts of interest.

**Data availability.** Data underlying the results presented in this paper are not publicly available at this time but may be obtained from the authors upon reasonable request.

### REFERENCES

- H. Fu and R. E. Cohen, "Polarization rotation mechanism for ultrahigh electromechanical response in single-crystal piezoelectrics," Nature 403, 281–283 (2000).
- G. Xu, H. Luo, P. Wang, H. Xu, and Z. Yin, "Ferroelectric and piezoelectric properties of novel relaxor ferroelectric single crystals PMNT," Chin. Sci. Bull. 45, 491–495 (2000).
- Y. Chen, K. Lam, D. Zhou, Q. Yue, Y. Yu, J. Wu, W. Qiu, L. Sun, C. Zhang, H. Luo, H. Chan, and J. Dai, "High performance relaxor-based ferroelectric single crystals for ultrasonic transducer applications," Sensors 14, 13730–13758 (2014).

- J. Martín-Sánchez, R. Trotta, A. Mariscal, R. Serna, G. Piredda, S. Stroj, J. Edlinger, C. Schimpf, J. Aberl, T. Lettner, J. Wildmann, H. Huang, X. Yuan, D. Ziss, J. Stangl, and A. Rastelli, "Strain-tuning of the optical properties of semiconductor nanomaterials by integration onto piezoelectric actuators," Semicond. Sci. Technol. 33, 13001 (2017).
- S. Baek, M. S. Rzchowski, and V. A. Aksyuk, "Giant piezoelectricity in PMN-PT thin films: beyond PZT," MRS Bull. 37(11), 1022–1029 (2012).
- X. Jiang, J. R. Yuan, A. Cheng, K. Snook, P. J. Cao, P. W. Rehrig, W. S. Hackenberger, G. Lavalelle, X. Geng, and T. R. Shrout, "Microfabrication of piezoelectric composite ultrasound transducers (PC-MUT)," in *IEEE Ultrasonics Symposium* (2006), pp. 922–925.
- Z. Lei, Y. Chen, G. Xu, J. Liu, M. Yuan, L. Zeng, X. Ji, and D. Wu, "Micromachining of high quality PMN-31%PT single crystals for high-frequency (>20 MHz) ultrasonic array transducer applications," Micromachines 11, 512 (2020).
- J. M. Cannata, J. A. Williams, Q. Zhou, T. A. Ritter, and K. K. Shung, "Development of a 35-MHz piezo-composite ultrasound array for medical imaging," IEEE Trans. Ultrason. Ferroelectr. Freq. Control 53, 224–236 (2006).
- Z. Li, J. Lv, X. Zhu, Y. Cui, and X. Jian, "Development of high frequency piezocomposite with hexagonal pillars via cold ablation process," Ultrasonics 114, 106404 (2021).
- J. Peng, C. Chao, J. Dai, H. L. W. Chan, and H. Luo, "Micro-patterning of 0.70Pb(Mg<sub>1/3</sub>Nb<sub>2/3</sub>)O<sub>3</sub>-0.30PbTiO<sub>3</sub> single crystals by ultrasonic wet chemical etching," Mater. Lett. 62, 3127-3130 (2008).
- I. A. Ivan, J. Agnus, and P. Lambert, "PMN-PT (lead magnesium niobate-lead titanate) piezoelectric material micromachining by excimer laser ablation and dry etching (DRIE)," Sens. Actuators A 177, 37-47 (2012).
- K. H. Lam, Y. Chen, K. Au, J. Chen, J. Y. Dai, and H. S. Luo, "Kerf profile and piezoresponse study of the laser micro-machined PMN-PT single crystal using 355 nm Nd:YAG," Mater. Res. Bull. 48, 3420–3423 (2013).
- S. I. Ashitkov, P. S. Komarov, E. V. Struleva, A. A. Yurkevich, and M. B. Agranat, "Dynamics of radiation emitted by metals exposed to femtosecond laser pulses," High Temp. 53, 887–890 (2015).
- D. Du, X. Liu, G. Korn, J. Squier, and G. Mourou, "Laser-induced breakdown by impact ionization in SiO<sub>2</sub> with pulse widths from 7 ns to 150 fs," Appl. Phys. Lett. 64, 3071–3073 (1994).
- P. C. Becker, H. L. Fragnito, C. H. B. Cruz, R. L. Fork, J. E. Cunningham, J. E. Henry, and C. V. Shank, "Femtosecond photon echoes from band-to-band transitions in GaAs," Phys. Rev. Lett. 61, 1647–1649 (1988).
- L. Jiang and H. L. Tsai, "Energy transport and material removal in wide bandgap materials by a femtosecond laser pulse," Int. J. Heat Mass Transfer 48, 487–499 (2005).
- G. Piredda, S. Stroj, D. Ziss, J. Stangl, R. Trotta, J. Martín-Sánchez, and A. Rastelli, "Micro-machining of PMN-PT crystals with ultrashort laser pulses," Appl. Phys. A 125, 201 (2019).
- T. Chen, A. Pan, C. Li, J. Si, and X. Hou, "Study on morphology of high-aspect-ratio grooves fabricated by using femtosecond laser irradiation and wet etching," Appl. Surf. Sci. 325, 145–150 (2015).
- B. Gao, T. Chen, Y. Chen, J. Si, and X. Hou, "Fabrication of through micro-hole arrays in silicon using femtosecond laser irradiation and selective chemical etching," Chin. Phys. Lett. 32, 107901 (2015).
- V. Khuat, Y. Ma, J. Si, T. Chen, F. Chen, and X. Hou, "Fabrication of micro-grooves in silicon carbide using femtosecond laser irradiation and acid etching," Chin. Phys. Lett. 31, 037901 (2014).
- A. Pan, J. Si, T. Chen, Y. Ma, F. Chen, and X. Hou, "Fabrication of high-aspect-ratio grooves in silicon using femtosecond laser irradiation and oxygen-dependent acid etching," Opt. Express 21, 16657–16662 (2013).
- Y. Ma, A. Pan, J. Si, T. Chen, F. Chen, and X. Hou, "A simple method for fabrication of high-aspect-ratio all-silicon grooves," Appl. Surf. Sci. 284, 372–378 (2013).
- J. Tauc, R. Grigorovici, and A. Vancu, "Optical properties and electronic structure of amorphous germanium," Phys. Stat. Solidi 15, 627–637 (1966).
- S. Dursun, H. Akyildiz, and V. Kalem, "PMN-PT nanoparticle/SnO<sub>2</sub> nanofiber heterostructures: enhanced photocatalytic degradation

- performance by ultrasonic wave induced piezoelectric field," J. Alloys Compd. 889, 161769 (2021).
- B. Dai, C. Lu, J. Kou, Z. Xu, and F. Wang, "Photocatalytic performance of PMN-PT@TiO₂ highly enhanced by alternative spatial electric field induced charge separation effect," J. Alloys Compd. 696, 988–995 (2017).
- A. Brodeur and S. L. Chin, "Ultrafast write-light continuum generation and self-focusing in transparent condensed media," J. Opt. Soc. Am. B 16, 637–650 (1999).
- D. von der Linde, K. Sokolowski-Tinten, and J. Bialkowski, "Laser-solid interaction in the femtosecond time regime," Appl. Surf. Sci. 109, 1–10 (1997).
- S. Eaton, H. Zhang, P. Herman, F. Yoshino, L. Shah, J. Bovatsek, and A. Arai, "Heat accumulation effects in femtosecond laserwritten waveguides with variable repetition rate," Opt. Express 13, 4708–4716 (2005).
- L. B. Kong, J. Ma, W. Zhu, and O. K. Tana, "Preparation of PMN-PT ceramics via a high-energy ball milling process," J. Alloys Compd. 336, 242–246 (2002).
- C. Ronchi and M. Sheindlin, "Melting point of MgO," J. Appl. Phys. 90, 3325–3331 (2001).
- K. P. Matabola, E. M. van der Merwe, C. A. Strydom, and F. J. W. Labuschagne, "The influence of hydrating agents on the hydration of industrial magnesium oxide," J. Chem. Technol. Biotechnol. 85, 1569–1574 (2010).
- E. W. Wescott, "The equilibrium between chlorine and plumbous and plumbic chlorides in aqueous solution," J. Am. Chem. Soc. 42, 1335– 1349 (1920).
- I. V. Mishakov, A. F. Bedilo, R. M. Richards, V. V. Chesnokov, A. M. Volodin, V. I. Zaikovskii, R. A. Buyanov, and K. J. Klabunde, "Nanocrystalline MgO as a dehydrohalogenation catalyst," J. Catal. 206, 40–48 (2002).

- 34. R. Gattass and E. Mazur, "Femtosecond laser micromachining in transparent materials," Nat. Photonics 2, 219–225 (2008).
- J. Song, X. Wang, X. Hu, Y. Dai, J. Qiu, Y. Cheng, and Z. Xu, "Formation mechanism of self-organized voids in dielectrics induced by tightly focused femtosecond laser pulses," Appl. Phys. Lett. 92, 092904 (2008).
- A. Borowiec and H. K. Haugen, "Femtosecond laser micromachining of grooves in indium phosphide," Appl. Phys. A 79, 521–529 (2004).
- M. Gertsvolf, H. Jean-Ruel, P. P. Rajeev, D. D. Klug, D. M. Rayner, and P. B. Corkum, "Orientation-dependent multiphoton ionization in wide band gap crystals," Phys. Rev. Lett. 101, 243001 (2008).
- H. Dachraoui, C. Oberer, and U. Heinzmann, "Femtosecond crystallographic experiment in wide-bandgap LiF crystal," Opt. Express 19, 2797–2804 (2011).
- V. Khuat, T. Chen, B. Gao, J. Si, Y. Ma, and X. Hou, "Uniform nanoripples on the sidewall of silicon carbide micro-hole fabricated by femtosecond laser irradiation and acid etching," Appl. Phys. Lett. 104, 241907 (2014).
- M. K. Bhuyan, F. Courvoisier, P. A. Lacourt, M. Jacquot, R. Salut, L. Furfaro, and J. M. Dudley, "High aspect ratio nanochannel machining using single shot femtosecond Bessel beams," Appl. Phys. Lett. 97, 081102 (2010).
- Q. Xie, X. Li, L. Jiang, B. Xia, X. Yan, W. Zhao, and Y. Lu, "High-aspect-ratio, high-quality microdrilling by electron density control using a femtosecond laser Bessel beam," Appl. Phys. A 122, 136 (2016).
- J. Del Hoyo, R. Meyer, L. Furfaro, and F. Courvoisier, "Nanoscale confinement of energy deposition in glass by double ultrafast Bessel pulses," Nanophotonics 10, 1089–1097 (2021).